Supporting Information

Kempf *et al.* 10.1073/pnas.0806563106

SI Text

Methods. A strain-free sample was immersed in *l*-He below the λ-point ($T \approx 2$ K) in an optical cryostat. The NMR probe included coils for multinuclear (^{69}Ga, ^{71}Ga, ^{75}As) excitation and $\mathbf{B}_0$ (246 mT) along the [001] crystal axis of a strain-free sample (7). For distinct $\mathbf{B}_0$ along [110] during t_1, we used an external electromagnet and adiabatic cycling of $\mathbf{B}_0$ between ($B_{001} = 246$ mT) and ($B_{110} = 57.6$ mT) (7). Near-bandgap (802.1 nm) optical excitation was provided by a logic-gated diode laser, and optical detection was via an 832 ± 5 nm bandpass filter.

The hyperfine imaging spectra of Fig. 2, and corresponding light-off reference (not shown), were acquired back-to-back during a 180-min run. For $t_{ONP} = 144$ and 240 ms, 4 spectra were averaged in the time domain, whereas others were single experiments. The CLSW-16 sequence with cycle duration, $t_c = 120$ μs, was used for maximum spectral width ($\Delta t_1 = t_c$), and using 3.45 and 4.00 μs $\pi/2$ times for the ^{71}Ga hyperfine and LQSE experiments, respectively. Corresponding optical-pulse arrangements yielded $b \approx 0.109$ and 0.2. Regardless of $t_{ONP}(^{71}\text{Ga})$, experiments had $t_{ONP} = 5.0$ s for ^{75}As (the LBD reference) and ^{69}Ga, with nucleus-specific ONP times set using selective saturation sequences as in Fig. 1. For LBD, typical spin-lock fields were ^{71}Ga (11 kHz, on resonance) and ^{75}As (10.8 kHz, 25 kHz above resonance). To avoid *l*-He loss from heating of the rf coils, LBD was stopped at 2.25 s, before full signal decay. All parameters were similar in experiments measuring relaxation times, the interfacial E field, or when ^{69}Ga was the signal nucleus. Additional details of instrumentation, sample handling, and POWER-NMR synchronization are described elsewhere (7).

POWER experiments incorporated an essential modification of CLSW-16 (not shown in Fig. 2*A*). Individual members of the 1st and 3rd (2nd and 4th) pairs of x or $\bar{x}$ pulses were shortened (lengthened) on each side by t_{mod}. This provided a homogeneous signal offset (ν_{off}) in t_1 (4, 8), and also yielded "2nd averaging" of the NMR Hamiltonian (9). Without this, unwanted error terms in $\bar{\mathcal{H}}$ can yield splittings 2- to 3-fold greater than the FWHM of a properly 2nd-averaged line shape (4, 7). Hyperfine and LQSE experiments used $t_{mod} = 200$ ns, yielding $\nu_{off} \approx 2.1$ and 1.3 kHz, a difference due to the distinct $\pi/2$ times used.

Finally, we note that, although not significant for the present application, magnetic inequivalence introduced by a perturbation may yield appreciable homonuclear J couplings in the effective Hamiltonian for POWER NMR. These could contribute to the linewidth, blurring the distribution of single-spin properties beyond the point spread function estimated from $\Delta\nu$ of the control spectrum without the perturbation. Here, neighbor-to-neighbor variations in hyperfine or LQSE interactions are (by far) sufficiently small such that ensemble $\Delta\nu$ of the light-off spectra match $\Delta\nu$ for all appreciable single-spin of contributions to light-on spectra. A distinct treatment for systems in which nearest-neighbor homonuclear J couplings are significant has been presented elsewhere (see ref. 19 of the main text).

Photoluminescence spectra and polarization. The PL spectrum of Fig. S2 *a* and *b* was obtained with an Ar^+ laser at 514.5 nm (Spectra Physics, model 2020) and a 1-m monochrometer (SPEX, model 1704) with 0.2-nm resolution. PL and polarization measurements in the ONMR apparatus (Fig. S2 *c* and *d*) were obtained by replacing the avalanche photodiode with a fiber-coupled optical spectrometer (Ocean Optics, model PC2000) with 1-nm resolution. Total PL spectra were collected without a λ/4 plate in the detection pathway. Collecting the σ_+ or σ_- components of PL (as opposed to their sum) was achieved by adding an appropriately oriented λ/4 plate to the detection pathway. Additional details are reported elsewhere (7).

As noted in the main text, we established that the *d* line of the *H* band is the ONMR signal carrier using optical filtering and polarization analysis. The 832 ± 5 nm filter diminished PL from the bulk exciton ($\rho = 0.06$) and *e* line ($\rho = 0.17$) features to small fractions (0.02 and 0.05, respectively) of collected *d* line intensity. Meanwhile, the BA_C transition contributed ≈0.75 of the PL, but showed $\rho = -0.04$, consistent with thermal spin ordering, and only a slight Hanle depolarization at transverse fields up to 5 mT, which indicates relative insensitivity to LBD. The *d* line, in contrast, had $\rho = 0.16$ that vanishes with application of a 5 mT transverse field, while contributing 0.23 of the filtered PL. The noted measurements of ρ are from fits to each PL line with σ_+ or σ_- detection (Fig. S2*d*), and were collected with the same $|\mathbf{B}_0| = 246$ mT as used in ONMR experiments.

Quantification of nuclear spin relaxation during optical excitation. As described in the main text, we determined $T_1^{hf}(0)$ and T_1^Q by recording the ONMR signal at $t_1 = 0$ as a function of t_{ONP} (0–30 s) and t_2 (0–2.25 s). In these experiments, ONP times for the reference nucleus (^{75}As) and nonsignal gallium isotope were fixed at 5 s by placement of selective saturation sequences during ONP. Two-dimensional fits used a simplified four-parameter (A_0, A_1, $T_1^{hf}(0)$, and T_1^Q) fit function. The model assumed $\rho_0\, T_1^Q \ll \rho_T\, T_1^{hf}(r_i)$, which is justified given that $(\rho_0/\rho_T) \approx 10^3$, the expectation (10) that $(T_1^{hf}(0)/T_1^Q) \approx 10^{-6}$, and our finding that contributions from $(r/a_0^*) > 3$ are negligible. In calculating the signals, summation over sites from $r = 0$–70 nm was adequately approximated by integration, which assumes continuous nuclear spin density. The fitting scheme with iterative descent to short-timescale data began with a fit to a full 2D dataset. Best-fit results from that were used as inputs for a subsequent fit to a truncated set with reduced maximum t_{ONP} and t_2 values. Truncation with input parameter guesses from the prior fit continued for execution of the process on a grid defined by the cross of sets $t_2^{max} = \{0.4, 0.6, 0.8, 1.0, 1.3, 1.6, 1.9, 2.25\}$ and $t_{ONP}^{max} = \{0.696, 1.176, 1.896, 3.960, 6.120, 8.640, 10.872, 12.600, 14.112, 17.352, 20.592, 24.480, 29.664\}$, with all values in seconds.

Finally, the integrated form of the fit function is insensitive to a_0^*. However, its success here as a model of the signal confirms the radial exponential distribution of electron spin density. Single exponentials in t_1 and t_2 for all r did not yield acceptable fits, also consistent with our nanoscale model of the signal.

The spatial resolution of hyperfine images. The radial resolution plotted in Fig. 4*B* is derived from

$$\Delta r = \left(\frac{d}{d\nu_{hf}}\, r(\nu_{hf})\right)\Delta\nu, \qquad \textbf{[S1]}$$

where $r(\nu_{hf})$ is obtained by solution of Eqs. **1** and **2** of the main text. Subsequent evaluation of Eq. **S1** yields

$$\Delta r = \left(\frac{a_0^*}{2}\,\frac{\Delta\nu}{\nu_{hf}(0)}\right)e^{+2r/a_0^*}. \qquad \textbf{[S2]}$$

The best-fit result ($\langle S\rangle = 0.15_3$) from the hyperfine distribution spectra yielded $\nu_{hf}(0) = 2.51$ kHz, whereas $\Delta\nu = 32$ Hz in the spectra of Fig. 4*A*. These specify the radial dependence of Δr plotted in Fig. 4*B*.

Measurement and calculation of the interfacial field. For LQSE-based measure of the interfacial E field, we ensured validity of the inactive-LQSE ($\mathbf{B}_0$ // [001]) as a control (Fig. S5) by cycling

reduced $|\mathbf{B}_0| = 57.8$ mT during t_1 but without altering orientation. This $|\mathbf{B}_0|$ value matched that used in the LQSE-active experiment with $\mathbf{B}_0 \,//\, [110]$. Time-proportional phase incrementation (TPPI) of pulses labeled ϕ_1 and ϕ_2 in Fig. S5*a* resulted in a net shift of the signal to 50 kHz (4, 11). Other experimental details follow from *SI Methods* above. In fitting the LQSE-active result with 3:4:3 quadrupole-split model to obtain $E_{001} = (1.2_6 \pm 0.0_7)$ kV/cm reported in the main text, we assumed uniform line width matching that observed [$(1.27_8 \pm 0.03_5)$ kHz] in the LQSE-inactive spectrum. Indistinguishable values (but greater uncertainties) in both E_{100} and the line width resulted when the latter was also implemented as a free parameter.

The AlGaAs/GaAs band structure corresponding to Fig. S6 was calculated numerically by using a self-consistent Schrödinger–Poisson (SP) solver. Relevant parameters included: a dielectric constant of 13.0 in each material, background *p*-type doping of 3×10^{14} cm^{-3}, a valence-band offset at the AlGaAs/GaAs interfaces of 35% of the total gap difference, and energy pinning at the surface (i.e., of the GaAs cap) and substrate of 0.7 eV, which corresponds to the mid-gap of GaAs. [The Schrödinger–Poisson solver used here accepts a dielectric constant no greater than 13.0, whereas the accepted value in GaAs is 13.1 (5). This difference is not expected to significantly impact our interpretation of the interfacial field and confined hole states.] The SP solver accounts for only one type of hole. However, because the degeneracy of heavy and light holes is removed at the interface, previous authors have neglected the lower-energy light-hole levels to calculate the interfacial subband states (12). Therefore, we assumed the GaAs heavy-hole mass, $m_{hh} = 0.465$, in units of the electron rest mass. The calculation was executed on a 1D grid with 0.2-nm spacing used from the surface to a distance of 60 nm beyond the heterojunction interface, whereas a 6-nm increment was used from that point out to the sample substrate. Fig. S6 shows the resulting profiles of the interfacial electric field (E_{int}^{100}) and the envelope wave functions of occupied discrete hole states.

Generation of empirical signal weights. Formal derivation of the empirical-weighting procedure outlined in Fig. S3 is general to any wave function, $\Psi(\mathbf{r})$, for the electronic state responsible for hyperfine shifts. Therefore, while the present application concerns a radial state, this weighting scheme is equally applicable to a variety of systems, including quantum wells and dots or trapped charges in biomolecular systems. Ultimately, the inputs required to generate the empirical weighting function, $A_{\text{E}}(\mathbf{r})$, are the POWER NMR hyperfine distribution spectrum, the underlying line widths of sites contributing to that spectrum, the explicit $|\Psi(\mathbf{r})|$, and corresponding average electron spin, $\langle S \rangle$.

Derivation begins with an expression for the hyperfine-distribution spectrum in t_1:

$$S(t_1) = \int d^3\mathbf{r} \left[\sum_j A_E(\mathbf{r})\, \delta(\mathbf{r} - \mathbf{r}_j) \cos(2\pi\nu(\mathbf{r})t_1) e^{-\Delta\nu(\mathbf{r})t_1} \right] \qquad \textbf{[S3]}$$

where

$$\nu(\mathbf{r}) \;=\; \nu_{hf} |\Psi(\mathbf{r})|^2 \qquad \textbf{[S4]}$$

is the position-dependent angular frequency of the hyperfine shift, ν_{hf} is the magnitude of the hyperfine Hamiltonian (Eq. **1** of the main text) at the maximum of $|\Psi(\mathbf{r})|^2$, and $\Delta\nu(\mathbf{r})$ is FWHM of the (presumed Lorentzian) frequency domain contribution from the nucleus at $\mathbf{r}$. Equation **S3** weights the signal with Dirac delta functions, $\delta(\mathbf{r} - \mathbf{r}_j)$, at nuclear sites $\mathbf{r}_j$.

If the line width, $\Delta\nu(\mathbf{r})$, is spatially uniform see *SI Methods* for counter examples.), then multiplication by $e^{+\pi\Delta\nu t_1}$ deconvolutes it and subsequent Fourier transformation yields

$$\tilde{S}_d(\omega_1) = \int d^3\mathbf{r} \left[\sum_j A_E(\mathbf{r})\, \delta(\mathbf{r} - \mathbf{r}_j) \times \frac{1}{\sqrt{2\pi}} \int_{-\infty}^{\infty} dt_1 (e^{+i2\pi\nu_1 t_1} \cos(2\pi\omega(\mathbf{r})t_1)) \right]. \qquad \textbf{[S5]}$$

Reexpressing the cosine in terms of complex exponentials and recognizing the Fourier-transform representation of Dirac delta functions (13),

$$\delta(2\pi(\nu(\mathbf{r}) \pm \nu_1)) = (2\pi)^{-1} \int_{-\infty}^{\infty} dt_1 e^{-i2\pi(\pm\nu(\mathbf{r}) - \nu_1)t_1} = (2\pi)^{-1} \delta(\nu(\mathbf{r}) \pm \nu_1), \qquad \textbf{[S6]}$$

enables conversion of Eq. **S5** to

$$\tilde{S}_d(\nu_1) = \frac{1}{\sqrt{8\pi}} \int d^3\mathbf{r} \left[\sum_j A_{\text{E}}(\mathbf{r})\, \delta(\mathbf{r} - \mathbf{r}_j) \times (\delta(\nu(\mathbf{r}) - \nu_1) \;+\; \delta(\nu(\mathbf{r}) + \nu_1)) \right]. \qquad \textbf{[S7]}$$

The appearance of two frequencies ($\pm\nu_1$) in Eq. **S7** results from Fourier transformation of a nonquadrature signal. Thus, we subsequently drop one as a noncontributor to the observed signal. This is further justified by the fact that hyperfine shifts from interaction with a single electronic state may not vary in sign among the ensemble of interacting nuclei.

In most cases, it suffices to reexpress Eq. **S7** as a function of a single scalar variable. In the present application, r completely specifies the spatial dependencies of $\nu(\mathbf{r})$ and $A_{\text{E}}(\mathbf{r})$ via the electronic envelope $\psi(r)$. (See Eqs. **1**, **2**, and **3**–**6** in the main text.) In another example, a quantum well with isotropic in-plane charge distribution, the envelope $\psi(z)$ would be appropriate, and $\{\nu(\mathbf{r}), A(\mathbf{r})\} \rightarrow \{\nu(z), A(z)\}$. General simplification of Eq. **S7** to a scalar variable is described elsewhere (4). In the specific case of a radial variable, we have

$$\tilde{S}_d(\nu_1) = \frac{1}{\sqrt{8\pi}} \int dr \left[\sum_j A_{\text{E}}(r)\, \delta(r - r_j)\, \delta(\nu(r) - \nu_1) \right]. \qquad \textbf{[S8]}$$

To extract $A_{\text{E}}(r)$, it proves useful to define

$$g(r) = \nu(r) - \nu_1 \qquad \textbf{[S9]}$$

and exploit the relationship (13)

$$\delta(g(r)) = \sum_k |g'(r_k)|^{-1} \delta(r - r_k), \qquad \textbf{[S10]}$$

where the summation is over all k for which $g(r_k) = 0$ and where

$$g'(r_k) = \left[\frac{d\nu(r)}{dr} \right]_{r = r_k} \qquad \textbf{[S11]}$$

is nonvanishing. Because there is a one-to-one relationship between r and ν, the only contributing terms in Eq. **S10** have $r_k = r(\nu_1)$. Thus, we obtain

$$\delta(\nu(r) - \nu_1) = \left| \left(\frac{d\nu(r)}{dr} \right)_{r = r(\nu_1)} \right|^{-1} \delta(r - r(\nu_1)). \qquad \textbf{[S12]}$$

Inserting this into Eq. **S8** and integrating the result yields

$$\tilde{S}_d(\nu_1) = \frac{1}{\sqrt{8\pi}} \sum_j{}' A_E(r(\nu_1)) \left| \left(\frac{d\nu(r)}{dr} \right)_{r=r(\nu_1)} \right|^{-1}, \quad \text{[S13]}$$

where priming the sum indicates limitation to sites where $r = r(\nu_1)$. Further, as no factors are indexed, the sum amounts to counting the number of these sites, which, for the radial case, is

$$N(r) = 4\pi\Omega^{-1} r^2 dr. \quad \text{[S14]}$$

Rearrangement of Eq. **S13** thus provides

$$A_E(r(\nu_1)) = \frac{1}{\sqrt{8\pi}} \left(\left| \left(\frac{d\nu(r)}{dr} \right)_{r=r(\nu_1)} \right| / N(r) \right) \tilde{S}_d(\nu_1). \quad \text{[S15]}$$

Finally, the desired single-spin, time-domain, empirical weighting function,

$$A_E(r) = \alpha r^{-2} e^{-2r/a_0^*} \tilde{S}_d(r), \quad \text{[S16]}$$

is obtained by using the radial dependencies of $N(r)$ (Eq. **S14**) and $\nu(r)$ (Eqs. **1** and **2** in the main text). The latter, along with the measured $\langle S \rangle$ is also required to convert, $\tilde{S}_d(\nu_1) \rightarrow \tilde{S}_d(r)$. All numerical prefactors are collapsed into the single constant α. Importantly, this is not a free parameter, but rather is set by scaling calculated spectra such that their amplitude at $t_1 = 0$ matches that of the observed spectrum. The empirical function is specific to the conditions used to obtain $\tilde{S}_d(r)$, such as the durations of ONP and the integrated detection period (t_2), optical polarization, alignment of the sample and temperature. The effect of t_{ONP} on the empirical weighting functions is shown in Fig. S3 *d* and *e*.

Discussion. ***Spin diffusion and spin-locked relaxation.*** As noted in the main text, our analysis of radially resolved, spin-locked relaxation data of Fig. 3 indicates an intermediate case in which the influence of spin diffusion is neither negligible nor uniformly fast. Observations indicate its increased influence with ν_{hf}, i.e., spin diffusion is most prominent in the small r region of the hyperfine distribution. This may be understood from Eqs. **1** and **2** of the article, which reveal coincident maxima at the center of $\Psi(r_i)$ for both $\nu_{hf}^2 \propto |H_{hf}|^2$ and the spatial rate of change in relaxation, $(\frac{\partial}{\partial r}(T_{1\rho}^{hf})^{-1} \propto \frac{\partial}{\partial r}|H_{hf}|^2)$. Thus, at large ν_{hf}^2 (i.e., $r \rightarrow 0$), diffusion over a given distance yields a more noticeable effect on $(T_{1\rho}^{hf})^{-1}$ than it does for small ν_{hf}^2. Conversely, diminishing effects result at sites at greater r with small, slowly varying hyperfine shifts. Also, as noted in the article, a linear fit to this regime ($\nu_{hf} \lesssim 200$ Hz) thus reveals $T_{1\rho}^B(^{71}\text{Ga}) = 4.8 \pm 0.4$ s, and, from a separate experiment, $T_{1\rho}^B(^{69}\text{Ga}) = 2.9 \pm 0.1$ s. Here, we note that the ratio (0.61 ± 0.06) of these background contributions is greater than expected (0.4) for purely quadrupolar relaxation. The observed ratio is quantitatively explained by a position-independent term that includes quadrupolar relaxation, but also a magnetic mechanism contributing 17% of $(T_{1\rho}^B(^{69}\text{Ga}))^{-1}$ and 47% of $(T_{1\rho}^B(^{71}\text{Ga}))^{-1}$. This is likely due to phase noise of the rf, as we noted a sensitivity of the rates to the rf source. Nevertheless, this detail in no way alters our subsequent analysis of hyperfine distributions, because decomposition of $T_{1\rho}$ into hyperfine and other terms is sufficient to allow quantitative modeling.

1. Brozel MR, Stillman GE (1996) *Properties of Gallium Arsenide* (Inspec, The Institution of Electrical Engineers, London).
2. Dargys A, Kundroths J (1994) *Handbook on Physical Properties of Ge, Si, GaAs and InP* (Science and Encyclopedia Publishers, Vilnius).
3. Reynolds DC, Collins TC (1981) *Excitons: Their Properties and Uses* (Academic, New York).
4. Kempf JG (2000) Probing quantum confinement at the atomic scale with optically detected NMR. PhD thesis (California Institute of Technology, Pasadena, CA).
5. Kittel C (1976) *Introduction to Solid State Physics* (Wiley, New York).
6. Paget D, Lampel G, Sapoval B, Safarov VI (1977) Low field electron-nuclear spin coupling in gallium arsenide under optical pumping conditions. *Phys Rev B* 15:5780–5796.
7. Kempf JG, *et al.* (2008) An optical NMR spectrometer for Larmor-beat detection and high-resolution POWER NMR. *Rev Sci Instrum* 79:063904.
8. Cho HM, Lee CJ, Shykind DN, Weitekamp DP (1985) Nutation sequences for magnetic resonance imaging in solids. *Phys Rev Lett* 55:1923–1926.
9. Pines A, Waugh JS (1972) Quantitative aspects of coherent averaging. simple treatment of resonance offset processes in multiple-pulse NMR. *J Magn Reson* 8:354–365.
10. Paget D (1982) Optical-detection of NMR in high-purity GaAs: Direct study of the relaxation of nuclei close to shallow donors. *Phys Rev B* 25:4444–4451.
11. Drobny G, *et al.* (1979) Fourier transform multiple quantum nuclear magnetic resonance. *Faraday Symp Chem Soc* 13:49–55.
12. Ossau W, Bangert E, Weimann G (1987) Radiative recombination of a 3D-electron with a 2D-hole in *p*-type GaAs/(AlGa)As heterojunctions. *Solid State Commun* 64:711–715.
13. Cohen-Tannoudji C, Diu B, Laloë F (1977) Quantum Mechanics. (Wiley, New York), Vol 2, pp 1468–1479.

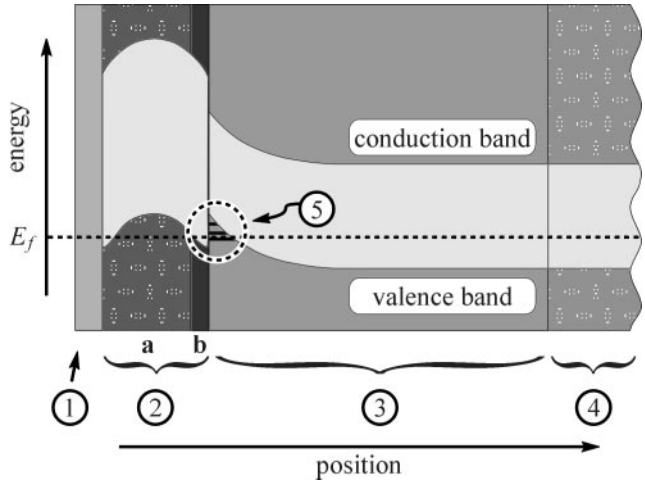

Fig. S1. Schematic of layered structure and energy bands of the $Al_xGa_{(1-x)}As/GaAs$ ($x = 0.36$) modulation-doped *p*-channel heterojunction sample grown by molecular-beam epitaxy. Layer 1 is a 21-nm GaAs surface cap, which provides chemical stability in air. Layer 2 is modulation-doped *p*-type $Al_xGa_{(1-x)}As$, in which the topmost 30 nm (a) is beryllium doped at 6×10^{17} cm^{-3} and the following 6.5 nm (b) is an undoped spacer. Layer 3 is the ''active'' layer of the sample and consists of 2,500 nm of undoped GaAs grown in the [001] direction on a GaAs substrate (layer 4). The Fermi energy E_F is in the GaAs gap near the valence band edge, whereas band bending yields hole-occupied discrete states in the interface notch (position 5). Optical excitation at 802.1 nm occurs in layer 3 only. Layer 1 is transparent because of perturbation of its band structure by surface effects and quantum confinement, whereas the gap of AlGaAs (layer 2) is well above the excitation energy.

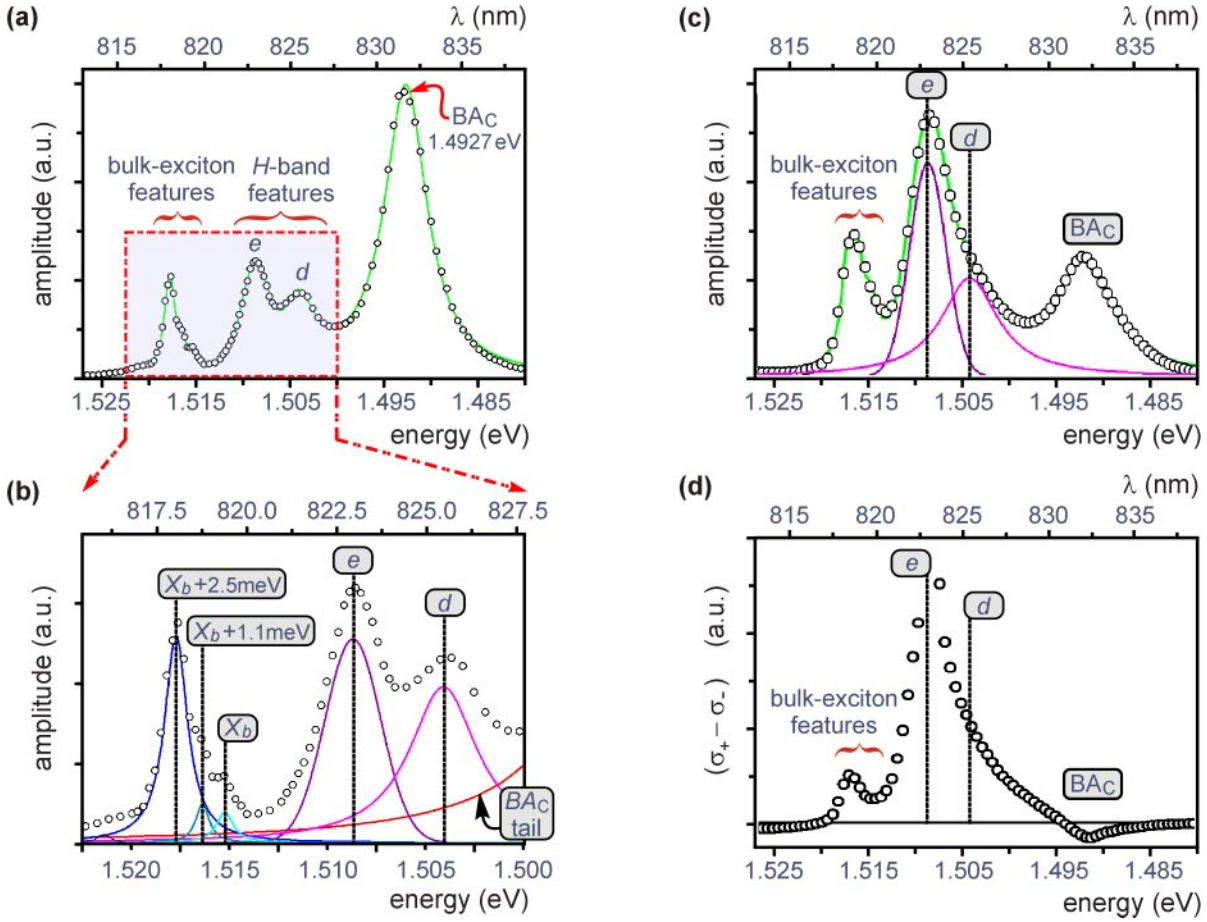

Fig. S2. The PL spectra the $Al_{0.36}Ga_{0.64}As$/GaAs heterojunction sample. (*a*) Spectrum (points) collected at $T \approx 4$–5 K with a 514 nm Ar^+ excitation source. The fit (line) consists of components detailed in *b*. (*b*) Expanded view from *a*, with individual components of the global fit. All components are Lorentzians, excepting the *e* line, which required a Gaussian. The band-to-carbon-acceptor (BA_C) and bulk exciton (X_b) at 1.493 and 1.5153 eV correspond to literature assignments (1, 2). The *e* and *d* lines are 6.5 and 11.0 meV below $E(X_b)$. (*c*) Spectrum collected in ONMR apparatus at $T \approx 2$ K in a 246.5 mT field mutually parallel to the sample growth direction and the propagation axis of the right circularly polarized (σ_+) excitation at 802.1 nm and 2.0 $\pm$ 0.5 W/cm^2. The global fit included the same components used in *a* and *b*. However, here, the intensity of *e* and *d* lines is increased relative to both bulk exciton and BA_C features. (*d*) Difference between the right (σ_+) and left (σ_-) CP components of sample PL, from which $\rho = (\sigma_+ - \sigma_-)/(\sigma_+ + \sigma_-)$ is determined. Spectra were collected as in *c*.

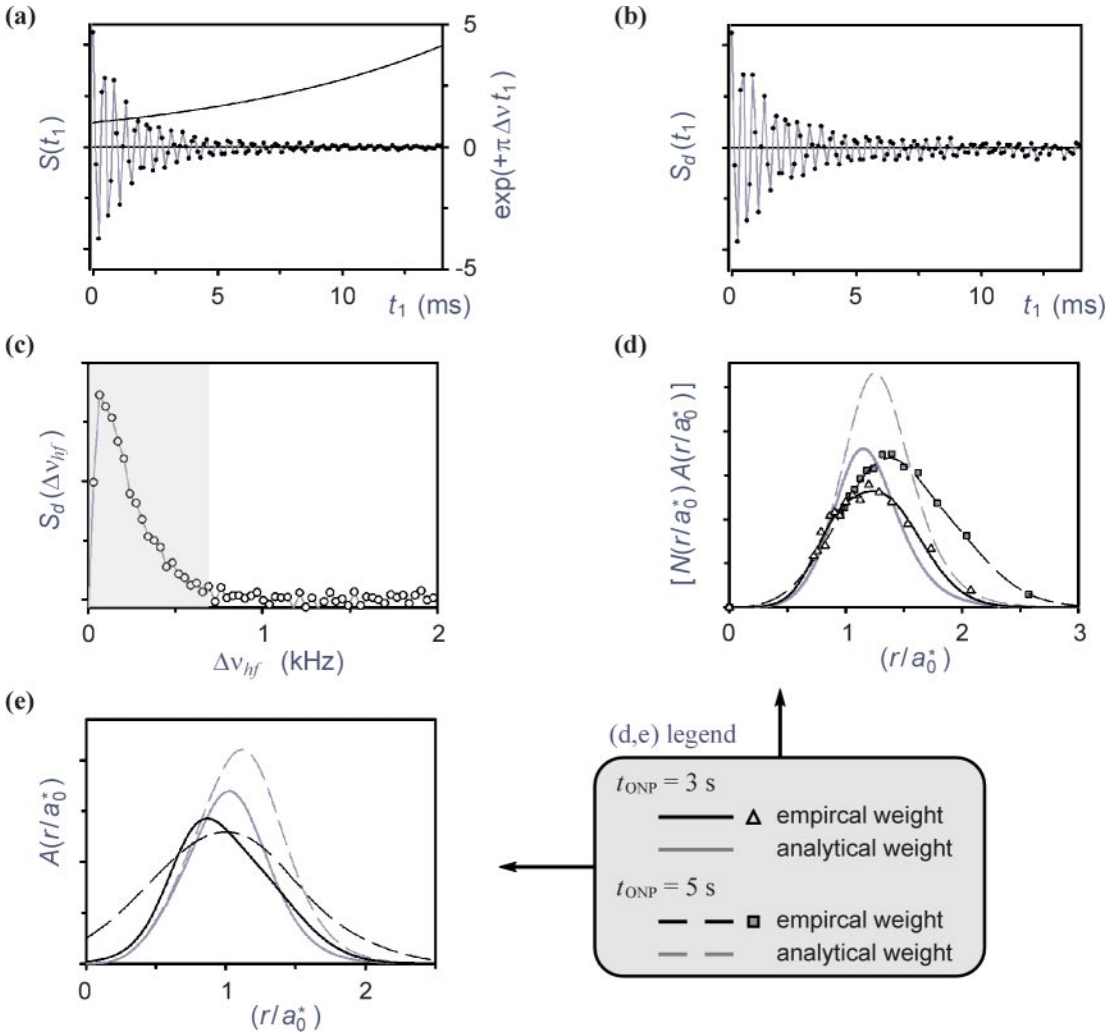

Fig. S3. Procedure for obtaining an empirical radial-weighting function from a hyperfine distribution spectrum. The $t_{ONP} = 3$ s data of Fig. 4 in the main text is treated, although *d* and *e* also include $t_{ONP} = 5$ s data for comparison. (*a*) Time-domain spectrum $S(t_1)$ and inverse decay, $e^{+\pi\Delta\nu t1}$, of corresponding light-off spectrum. (*b*) Linewidth-deconvoluted time-domain, $S_d(t_1)$, which is the product of the plots in *a*. Lines in *a* and *b* merely connect points. (*c*) Linewidth-deconvoluted frequency domain, $S_d(\Delta\nu_{hf})$, resulting from Fourier transformation of *b* and referral of $\Delta\nu_{hf} = 0$ to the light-off spectrum. Data in the shaded region ($\Delta\nu_{hf} \lesssim 0.65$ kHz) are used to determine empirical signal weights. (*d*) Radial weighting function, $[N(r/a_0^*)\,A(r/a_0^*)]$, for the total ONMR signal, a product of radially dependent nuclear counts and single-spin weights. Data were obtained by conversion of amplitudes and frequencies in (c) to weights and radial positions using Eq. **S16** and Eqs. **1** and **2** of the main text with $\langle S\rangle = 0.15$ and parameters from Table S1. The empirical weighting function is a fit of two gaussians to these data and a point inserted at $r = 0$, where the signal vanishes. The analytical function is the product of r^2 and the $t_1 = 0$ amplitude of Eq. **3** (and Eqs. **4**–**6**) of the main text. Normalization here yielded the same total intensity as the empirical function. (*e*) Single-nucleus radial-weighting functions, which are the product of weights in *d* and $N(r)^{-1} \propto r^{-2}$ (see Eq. **S16**).

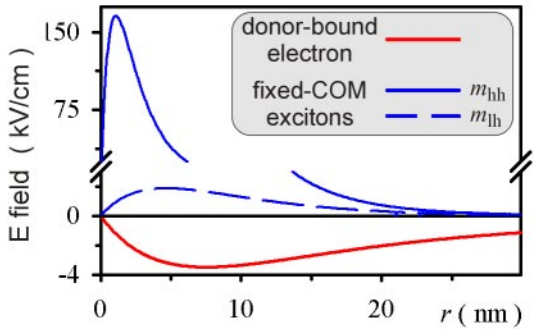

Fig. S4. Calculated electric-field profiles of localized radial electronic states that we considered as models for the ONMR signal carrier. Note the change in scale after the break in the vertical axis. Simulations of the LQSE POWER NMR spectrum (Fig. 5) in terms of a fixed-COM excitonic state assumed the heavy-hole E field distribution. This corresponds to the ratio $m_e/m_h = 0.15$ of electron-to-hole effective masses in GaAs (3), yielding a hole Bohr radius of 1.56 nm. Simulations with light-hole or mixed heavy/light hole excitons yielded similar χ^2 values. However, the exciton-dissociation limit of heavy-hole excitons is most consistent with our observation of a 1.2 kV/cm interfacial field at the sites of excitonic recombination. Details of the straightforward electrostatic calculations that yielded these results are described in ref. 4 of *SI*.

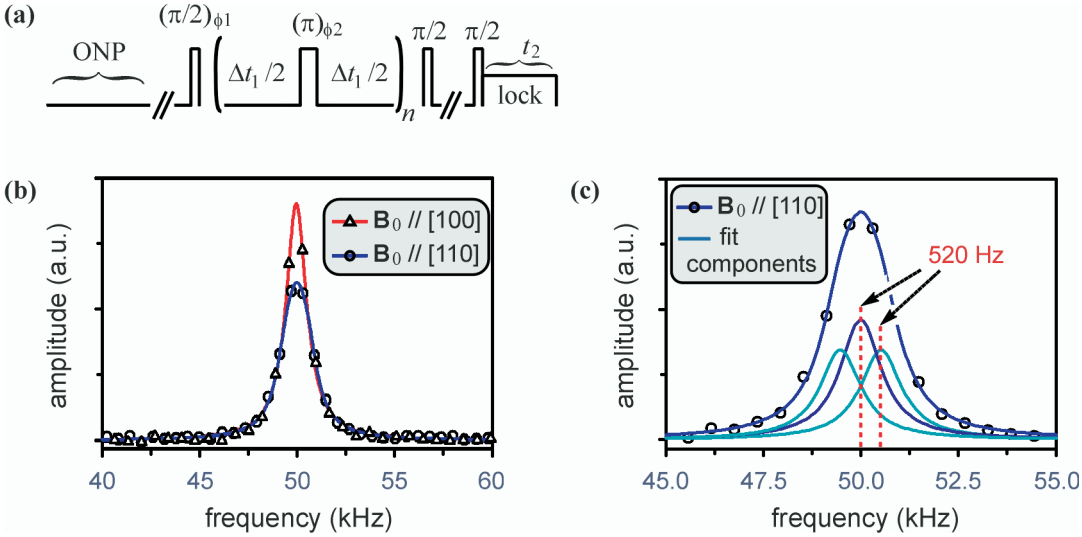

Fig. S5. Measurement of the interfacial electric field at the sites of *d*-line recombination. (*a*) ONMR spin-echo pulse sequence with delays about t_1 to accommodate adiabatic reorientation of B_0 (and spins aligned with it) between the [001] and [110] crystal axes. (*b*) ^{71}Ga spectra with inactive (B_0 // [001]) or active (B_0 // [110]) LQSE during NMR evolution. Points and lines are data and Lorentzian fits. (*c*) Expanded view of the LQSE-active spectrum with separate plots of components in the fitting function, a 3:4:3 quadrupole triplet with a symmetric 520 Hz splitting that is linear in the interfacial E field. This corresponds to $E_{[001]} =$ (1.26 ± 0.07) kV/cm (4).

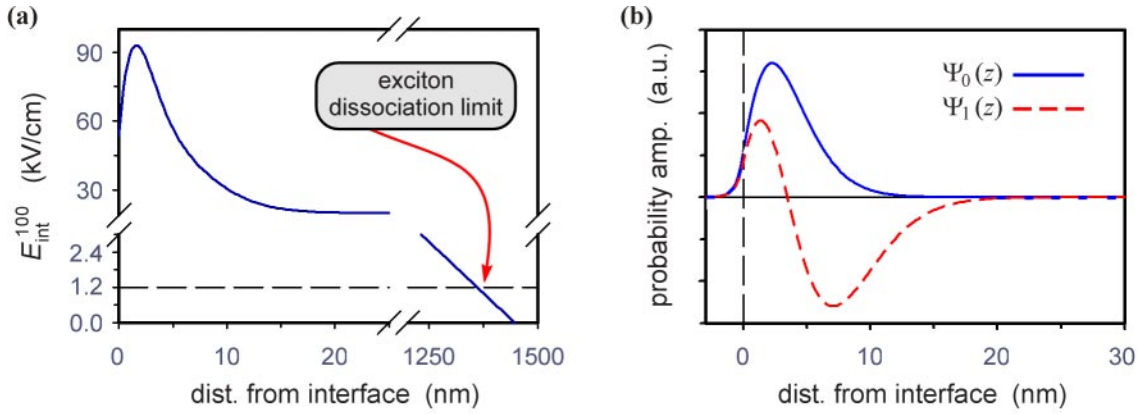

Fig. S6. Schrodinger–Poisson calculation of the interfacial electric field and interfacial states. (*a*) Calculated 1D profile of the interfacial E field (E_{int}^{001}) as a function of distance from the AlGaAs/GaAs interface on the GaAs side. Note the changes in scale at each break. (*b*) The normalized envelope wave functions of corresponding occupied interfacial hole states. If the *H*-band luminescence were due to the recombination of free electrons with these hole states, then the field profile of *a* predicts $E_{int}^{001} \approx 25$ kV/cm at the recombination sites. This starkly contrasts with the ≈1.2 kV/cm dissociation-limited field for excitonic recombination, which, as indicated in *a*, corresponds to a >1-μm distance from the interface.

Table S1. Constants and experimental parameters used in our simulation of POWER NMR hyperfine distribution spectra (Fig. 4, main text)

Constant or parameter	Units	^{71}Ga	^{69}Ga	Source / justification
$T_1^{hf}(0)$	ms	16	90	*
$T_{1\rho}^{B}$	s	4.8	2.9	*
a_0^*	nm	10.37	same	*
a	nm	0.565	same	Kittel (5)†
Ω	10^{-29} m^3	4.51	same	†
d_i	10^{31} m^{-3}	5.8	same	Paget *et al.* (6)
γ_n	MHz / T	12.98	10.22	—
Γ	none	1	same	*
b	none	$0.1091\bar{6}$	same	‡
ν_{off}	kHz	2.119_5	—	§
$\Delta\nu$	Hz	32.3	—	§

*Measurement of $T_1^{hf}(0)$ and $T_{1\rho}^{B}$ and justification for Γ and a_0^* are described in the main text.
†The GaAs lattice constant a determines the unit cell volume, $\Omega = (a^3/4)$.
‡Parameters of the CLSW-16 sequence determine b, the POWER NMR optical duty factor.
§A lorentzian fit to the light-off spectrum determined the $\Delta\nu_{hf} = 0$ reference (ν_{off}) and the uniform line width ($\Delta\nu$) used to calculate single-nucleus contributions to POWER NMR hyperfine distribution spectra.

Table S2. The χ^2 minima resulting from grid search over $\langle S \rangle$ and A_0, where optimal parameters are given for minimization at each t_{ONP}

t_{ONP}, ms	Best χ^2	$\langle S \rangle_{min}$	$(A_0)_{min}$	χ^2 at t_{ONP} = 144 ms minimum
144	1.0_0	0.15_3	0.78_0	1.0_0
240	1.2_6	0.15_0	0.77_6	1.2_6
720	1.5_9	0.14_8	0.83_0	1.8_2
3,000*	4.3_1	0.12_2	0.86_0	12.4_9

The last column provides the χ^2 value for simulations at each t_{ONP} using parameters in the top (t_{ONP} = 144 ms) row. Subscripted first insignificant digits give a sense of variation from fit to fit. Coarse and fine grids were used to cover the ranges: (*i*) $\langle S \rangle$ = [0.050, 0.395] and A_0 = [0.20, 1.25] with increments 0.01 and 0.05; and (*ii*) $\langle S \rangle$ = [0.125, 0.174] and A_0 = [l0.65, 0.85] with increments 0.0025 and 0.01.
*The χ^2 minimum for t_{ONP} = 3 s was determined in a coarse grid search only.